Research Square

Preprints are preliminary reports that have not undergone peer review.
They should not be considered conclusive, used to inform clinical practice,
or referenced by the media as validated information.

Multi-Moiré Networks in Engineered Lateral Hetero-Bilayers: Programmable Phononic Reconfiguration and Second Harmonic Generation

Prasana Sahoo

prasana@matsc.iitkgp.ac.in

Indian Institute of Technology Kharagpur https://orcid.org/0000-0001-6316-7842

Suman Chakraborty

Indian Institute of Technology Kharagpur

Frederico Sousa

Universidade Federal de Minas Gerais https://orcid.org/0000-0001-7974-9548

Chakradhar Sahoo

Aarhus University

Indrajeet Prasad

Department of Physics, Indian Institute of Technology Goa

Shneha Biswas

Department of Physics, Indian Institute of Science Education and Research Tirupati

Purbasha Ray

Indian Institute of Technology Kharagpur,

Biswajeet Nayak

Indian Institute of Technology Kharagpur,

Rafael R Rojas-Lopez

Departamento de Física, Universidade Federal de Minas Gerais https://orcid.org/0000-0002-2665-8148

Baisali Kundu

Indian Institute of Technology Kharagpur,

Alfred Jones

Aarhus University https://orcid.org/0000-0002-7930-0967

Jill Miwa

Department of Physics and Astronomy, Aarhus University

Søren Ulstrup

Aarhus University https://orcid.org/0000-0001-5922-4488

Sudipta Dutta

Department of Physics, Indian Institute of Science Education and Research Tirupati

Santosh Kumar
Indian Institute of Technology Goa https://orcid.org/0000-0001-7070-057X
Leandro Malard
Universidade Federal de Minas Gerais
Gopal Pradhan
Department of Physics, School of Applied Sciences, KIIT Deemed to be University

Article

Keywords:

Posted Date: August 14th, 2025

DOI: https://doi.org/10.21203/rs.3.rs-6546250/v1

License: This work is licensed under a Creative Commons Attribution 4.0 International License.
Read Full License

Additional Declarations: There is **NO** Competing Interest.

Abstract

Moiré-engineering in two-dimensional (2D) transition metal dichalcogenides (TMDs) offers precise control over correlated quantum phenomena, including moiré-excitons, quantum light sources, light-driven ferromagnetism, bosonic crystal, excitonic Mott-insulator, and photon-momentum controlled Hall effect. However, most studies rely on exfoliated flakes, limiting scalability and structural control. Here, we report a scalable multi-moiré platform formed by vertically stacking chemical vapor deposition-grown monolayer lateral heterostructures of TMDs, integrating four distinct moiré networks in a single 2D flatland. Systematic tuning of twist angle (θ) and material degrees of freedom reveals the intriguing phonon and exciton dynamics through Raman spectroscopy, photoluminescence (PL), micro-scale angle-resolved photoemission spectroscopy, and second-harmonic generation (SHG) measurements. A universal lattice relaxation mechanism is identified, evolving from rotational reconstruction (θ < 8°) to volumetric dilation (θ > 8°), with phonon renormalization influenced by interfacial transition metal chemistry. At small twist angles, the selectivity of strain on mechanically softer crystal follows in-plane phonon frequency engineering to a reduction of valley polarization (at 5K). The strain predominantly affects the top layer at larger twist angles with subsequent out-of-plane phonon linewidth broadenings owing to its epitaxial pseudomorphic epitaxial pattern. Angle-aligned hetero-bilayers exhibit Davydov-splitting in MoS2, a signature of symmetry breaking and distinctness from strain. Further SHG responses reveal an interplay between strain, orbital overlap, and excitonic resonance offsets work in tandem to fine-tune nonlinear optical responses. Complementary theoretical investigations support these observations, linking electronic band structure, phase delay variations, and interlayer coherence. These insights advance the design of programmable multi-moiré architectures for opto-straintronics, sensing, and integrated on-chip quantum photonics applications.

Introduction

Integrating diverse two-dimensional (2D) atomic crystals enables programmable moiré systems with unconventional electronic, optical and magnetic properties, where interlayer rotation, van der Waals (vdW) spacing, and interfacial elements govern orbital interactions, hybridization, and coupled functionalities[1–6]. While homogeneous stacking allows precise twist-angle control over electronic, optical, and valley properties, heterogeneous stacking exploits synergistic properties of materials and lattice mismatch, creating strong moiré landscapes and localization effects[7–9]. These approaches unlock exciting opportunities in band and dielectric-environment engineering to design proximity effects for multi-functional applications. Especially in transition metal dichalcogenides (TMDs) moiré systems, high-symmetry sites exhibit varying potential energies, with interlayer and in-plane interactions driving domain reconfiguration to minimize stacking energy[10]. This coupling-induced lattice relaxation generates controlled 2D hetero-strain, enabling quantum transport engineering[11], exciton localization[10], dipolar excitonic circuitry[12], emergence of flat bands[13], 1D moiré patterns[14], and chiral phonons[15]. These quantum-correlated phenomena are essential for designing excitonic lattices, polarization-sensitive optoelectronics, site-specific arrays of single photon emitters, and topological materials[5].

Probing the moiré superlattice structure and its associated heterostrain is crucial for tailoring phonons, excitons, and their collective behavior, which requires a comprehensive understanding of 1) moiré periodicity-dependent structural reconstruction and strain profile, 2) choice of moiré materials and associated lattice dynamics, and 3) moiré effects on optical excitations. Prior studies on 2D TMDs hetero-bilayer focused on moiré physics at specific twist angles, primarily exploring electronic and excitonic quantum phases[16–20]. However, systematic investigations into twist-angle and material-driven phonon renormalization and symmetry-controlled optical excitations like valley polarization and second harmonic generation (SHG) remain limited[21]. Recently, the importance of phonon dispersion in controlling electronic to thermal properties has been probed in twisted graphene systems[22]. In addition, understanding these effects is crucial for correlating 2D heterostrain from lattice relaxation and heterogeneity-driven complex structural interference to truly harness moiré functionalities in heterogenous moiré networks of TMDs. Moreover, although excitonic states are widely investigated[23–25], a systematic understanding of moiré-periodicity-tunable phonon spectra is still needed.

Phonon dynamics could offer a non-destructive approach for imaging atomic[3,21,26] and spectroscopic properties of moiré systems, enabling possibilities in designing quantum phononic devices, including acoustic band engineering, quantum transducer, acoustic filters, modulators[27–30], phonon Hall effects[31] and chiral-phonon-Berry physics[15,32]. Moiré-driven lattice reconfiguration allows effective tuning of symmetry alongside phonon engineering, leading to strong nonlinear effects. Despite extensive studies on nonlinear electronic quantum phases[2,33] in moiré materials, the controlling parameters governing elementary optical excitations, including SHG, remain unclear. Additionally, the twist angle-dependent nonlinear optical process as a synergistic effect of band offset, strain, and orbital characteristics to control interlayer coherence can be probed via SHG.

Extending moiré engineering to a self-assembled, multi-domain platform remains challenging with mechanically exfoliated samples. Understanding commensurate and incommensurate atomic registry-driven phenomena over tens of micrometers in as-synthesized 2D TMDs is crucial for practical device integration. This study investigated phonon dynamics across a wide range of twist angles (0º to 60º) in heterogeneous lateral hetero-bilayers (LHBs) of MoS_2-WS_2 and $MoSe_2$-WSe_2 monolayer (1L) lateral heterostructures (LHSs), grown via scalable chemical vapor deposition (CVD), using low- and high-frequency Raman spectroscopy. Vertical stacking of LHSs forms four distinct heterogeneous LHBs, such as WS_2/WSe_2, WS_2/$MoSe_2$, MoS_2/$MoSe_2$, and MoS_2/WSe_2, within a single sample, enabling scalable integration of four moiré networks, all-in-one 2D flatland. The correlation of lattice vibrations and micro-scale angle-resolved photoemission spectroscopy (μARPES) measurements revealed the critical roles of twist angle and material engineering in interlayer coupling strength, structural reconstruction, local torsional strain, volumetric strain, charge transfer and symmetry, a non-destructive approach elucidating new opportunities for controlling optical excitations. Vibronic responses indicate universal lattice relaxation modes across coupling regimes, while valley polarization measurements confirmed the signature of 2D heterostrain-induced chiral phonons. SHG studies further clarified the limited

understanding of the role of interlayer coupling, excitonic resonance offsets, and strain on nonlinear optical modulation, bridging gaps in lattice and optical excitation dynamics within moiré systems.

Results and Discussion

Water-assisted edge-epitaxial CVD growth of MoS_2-WS_2 and $MoSe_2$-WSe_2 LHSs ensured coherent crystal orientation (Experimental Section, Fig. S1)[34,35]. Four pockets of moiré networks are formed within a single 2D flatland via hetero-stacking of LHSs (Fig. 1a). Monolayer MoS_2-WS_2 LHS was transferred directly on as-synthesized 1L $MoSe_2$-WSe_2 LHS with controlled twist angles (Figs. 1b,S2). Optical microscope image (Fig. 1b) and corresponding spatially-resolved Raman spectral-intensity mapping (Fig. 1c) of LHBs confirm the spatial distribution of TMD domains within moiré networks and uniform coupling over several microns. Polarization-resolved SHG (Fig. 1d) and spatial SHG mapping (Fig. 1e) of LHBs with a twist angle of 2.7º show the spatial distribution of SHG intensity across individual TMDs and moiré networks. The difference in SHG intensity between 1L TMDs and the moiré networks within LHBs further confirms this interfacial nature of moiré coupling. A schematic representation of four pockets of moiré potentials (Fig. 1f) and High-Angle Annular Dark-Field Scanning Transmission Electron Microscopy (HAADF -STEM) Z-contrast image of stacked LHBs (Fig. 1g) illustrate the formation of distinct moiré networks across the 1D interfaces. To investigate the effect of material degree of freedom on interlayer hybridization, μARPES was performed on MoS_2/$MoSe_2$ and MoS_2/WSe_2 LHBs with ~2º twist (Figure 1h). The energy–momentum-resolved band structures exhibit sharp linewidths and clear spin-orbit splitting at the K-point, confirming the high quality of the CVD-grown heterostructures (Figs. 1h,S3). The energy distribution curves (EDCs) at the K-point, corresponding to the three individual 1L TMDs and their heterobilayers, further revealed distinct band features and splittings (Fig. S3). A detailed analysis of the Γ-point EDC spectra was conducted to examine hybridization and interlayer coupling (Fig. 1i). In the MoS_2/$MoSe_2$ and MoS_2/WSe_2 hetero-bilayers, the bands shifted towards Fermi-level by approximately 560 meV and 480 meV respectively compared to their isolated monolayers. Whereas, MoS_2 bands show negligible energy shifts. Notably, for MoS_2/$MoSe_2$, the hybridized band emerged approximately 80 meV lower in energy than that observed in MoS_2/WSe_2. This energy difference at the Γ-point confirms that MoS_2/$MoSe_2$ exhibits enhanced interlayer hybridization and stronger interlayer coupling than MoS_2/WSe_2 at the same twist angle[36].

Coupling Characteristics:

The Raman spectra of individual 1L WS_2 and WSe_2, compared with their hetero-bilayers stacked at different twist angles (Fig. 1j), reveal a systematic evolution of phonon modes linked to interlayer interaction and their modification with moiré periodicity. For pristine 1L WS_2, the peak at ~27.4 cm^{-1} corresponds to E^2_{2g} or quasi-breathing modes due to resonance of *B*-exciton in WS_2 with laser excitation (Figs. 1j;i)[37], while slight shifts, increasing

intensity and broadening in hetero-bilayers indicate the emergence of the layer breathing mode (LBM) in WS_2/WSe_2 and $WS_2/MoSe_2$. Clear LBMs are also observed in $MoS_2/MoSe_2$ and MoS_2/WSe_2 (Fig. S4a). Additionally, a 40-45 cm^{-1} peak in the low-frequency regime appears in small-twist-angle samples, presumably originating from the moiré phonon due to Brillouin zone folding of the moiré lattice (Figs. 1j;i). In the high-frequency region, while the Raman spectrum of a vdW heterostructure primarily consists of individual 1Ls, a new broad peak emerged at ~309 cm^{-1} for all the angles that can be assigned to collective excitation of the B_{2g} mode of bilayer (2L)-WSe_2 and [*LA(M)+TA(M)*] of 2L-WS_2 for the WS_2/WSe_2 system (Figs. 1j;iii). Similar homo-bilayer-like phonon modes appear in the other hetero-bilayer systems (Fig. S4b-d). The point group symmetry in 2D TMDs transit from D_{3h} (monolayer) and D_{3d} (homo-bilayer) to C_{3v} in hetero-bilayers, enabling Raman-active phonon modes otherwise forbidden in 1Ls. The presence of LBM, moiré phonons, and homo-bilayer characteristics in the Raman spectra of the moiré LHBs confirms interlayer interaction or coupled hetero-layers. Simulated phonon dispersion further supports an intense mixing of lower optical and higher acoustical modes due to interlayer coupling (Fig. S5).

Moiré Driven Phonon Renormalization and Volumetric Dilation:

In the high-frequency regime, in-plane intralayer vibrations E^1_{2g} and *2LA(M)* reveal insights into twist-driven lattice dynamics and strain in 2D vdW heterostructures. In twisted homo-bilayers of TMDs, phonon renormalization is linked to atomic reconstructions and local strain, peaking within 3º<θ<4º as the structural transitions from relaxed to rigid regime[26]. For 1L-WSe_2, a degenerate $A_{1g}$and E^1_{2g} peak appears at ~250.4 cm^{-1}, with *2LA(M)* at ~262 cm^{-1} (Fig. 1e;ii).While WS_2 shows a broad peak at ~353 cm^{-1}, assigned as *2LA(M)* and E^1_{2g}(Fig. 1e;iv). For WS_2/WSe_2,phonon renormalization of the *2LA(M)* mode of WSe_2 exhibits: 1) a redshift of ~4-5 cm^{-1} for θ<3°, 2) constant between 8°<θ<50° with ~2 cm^{-1} redshift as compared to 1L, and 3) a ~4 cm^{-1} redshift at 60º (Fig. 2a). The *2LA(M)* mode of WSe_2 usually softened by ~2 cm^{-1} in 2L compared to 1L due to increased dielectric screenings, reducing the bond strength. The pronounced redshift for θ<3° and θ~60° suggests torsional strain arising from interlayer forces and in-plane bonding-driven atomic reconstruction. Conversely, the $2LA(M)+E_{2g}$ mode of WS_2 redshifts by ~2 cm^{-1} up to 5º but remains insensitive to large twist angles (Fig. 2a), attributed to increased dielectric screening. The selective torsional strain effect on WSe_2, but not WS_2,can be attributed to the higher shear strength of WS_2 (Table S1). Therefore, the degree of reconfiguration of the *2LA(M)* mode of WSe_2 in WS_2/WSe_2 indicates significant atomic reconstruction below θ<3°, extending up to 8°.

In $MoS_2/MoSe_2$ andMoS_2/WSe_2, the E^1_{2g} mode of MoS_2 (Figs. 2b,c) is highly sensitive to small twist angle, whereas the E^1_{2g}mode of $MoSe_2$ and *2LA(M)* of WSe_2 remain unaffected. This contrast correlates with the lower shear strength of MoS_2 compared to $MoSe_2$ and WSe_2 (Table S1). A splitting (~3 cm^{-1}) of the E^1_{2g} mode of MoS_2 into E^+_{2g} and $E^-_{2g}$is observed, peaking at ~1° and ~0.5° for

$MoS_2/MoSe_2$ andMoS_2/WSe_2, respectively, indicating persistent torsional strain. The strain is maximized within 0°<θ<3º for $MoS_2/MoSe_2$ and 0°<θ<1° for MoS_2/WSe_2, highlighting the importance of choice of different transition metals on interfacial characteristics. Higher interlayer coupling in $MoS_2/MoSe_2$ compared to MoS_2/WSe_2, combined with global interlayer rotation, governs hybridization and reconstruction. For 8º<θ<50º, the E_{2g} mode of MoS_2 redshifts ~ <2 cm^{-1} than its 1L value (Figs. 2b,c) due to dielectric screening and reduced strain in the hetero-bilayers. A similar strain-driven lattice dynamics profile is observed in $WS_2/MoSe_2$, where the splitting and peak position variation of the E_{2g} mode of $MoSe_2$ and its lower shear strength correlates to twist angle effects (Fig. 2d).

The relative interlayer energy at different stacking symmetry domains, such as AA and AB, allows lattice relaxation via intralayer local rotational reconstruction to interlayer global rotation. Due to a slightly higher interlayer gap, AA stacking has higher energy than AB (BA), leading to increased AB (BA) domain area and shrinkage of AA stacking sites in the relaxed configuration. This results in a non-uniform distribution of local hetero-strain in the respective stacking sites. Strain-induced crystal deformation breaks the symmetry and strongly modulates the phonon modes at the small twist angle with large moiré periodicity. As moiré periodicity decreases at higher twist angles, the system is expected to become rigid. However,

a striking feature in the out-of-plane optical phonon mode A_{1g} isobserved. While its peak position weakly depends on strain, its linewidth broadens in WSe_2 and WS_2 (Fig. 3a). This suggests lattice relaxation can still occur at large twist angles without following atomic reconstruction, evident from the absence of strain effect on in-plane modes. At large twist angles, instead of atomic reconstruction, stacking-dependent local volumetric dilation[38] may occur, even with minimal local variation in the interlayer distance profile. Domains with lower (/higher) stacking energy undergo positive (/negative) dilation to reduce (/increase) the lattice mismatch. Such rearrangement breaks crystal symmetry, activating otherwise forbidden phonon modes in the 1L limit without persistent high local strain. The volumetric strain from dilation is weaker than the torsional strain from atomic reconstruction, affecting linewidth rather than phonon frequency. This effect is more pronounced in WS_2, where a change in linewidth broadening ($\Delta\omega$) compared to 1L exceeds 1 cm^{-1}, while in WSe_2, the $\Delta\omega$ remains within 0.4 cm^{-1}. Despite the higher in-plane mechanical strength of WS_2, the local volumetric strain remains robust on its top layer due to the epitaxial nature of the dilational effect. Similar to WS_2/WSe_2, the A_{1g} mode of MoS_2 exhibits fuzziness in the line shape across all twist angles in both systems (Figs. 3b,e), whereas $MoSe_2$ (Fig. 3d) and WSe_2 remain largely unaffected, as volumetric strain primarily concentrates in top layers.

For $MoS_2/MoSe_2$, A_{1g} mode in MoS_2 exhibits a splitting of ~3 cm^{-1} at twist angles of ~0.5° and ~60° (Fig. 3c), attributed to strong local strain and simultaneously electron-doping due to efficient charge transfer from $MoSe_2$. These perturbations break crystal symmetry, leading to “Davydov splitting”[39,40]— a phenomenon typically observed under resonant excitation in 2L and multilayer MoS_2. For *3R* (~0°) and *2H* (60°) stacking, the intensity ratio of the two modes reverses, indicating a stacking-dependent effect.

A similar Davydov splitting is observed in MoS_2/WSe_2 but is absent at *2H* (60°) stacking, likely due to higher electron-phonon coupling[41] in WSe_2 at 60° than 0º, which reduces electron transfer to MoS_2, weakens interlayer coupling and suppresses distinct energy level splitting. Strain plays a crucial role in maintaining this splitting and inducing chiral physics. Additionally, the lower intensity of the LBM mode in MoS_2/WSe_2 compared to $MoS_2/MoSe_2$ further confirms that changing transition metal at the interface weakens interlayer coupling (Fig. S6), as demonstrated by μARPES. A similar volumetric dilational effect with twist angle is observed on the lattice dynamics of $WS_2/MoSe_2$, correlating A_{1g} linewidth variation in both layers (Fig. 3f).

Twist and Material Controlled Phonon Intensity Engineering:

Understanding the effect of orientations between heterogeneous 2D TMDs on the phonon mode intensity variation and band profile is crucial. The A_{1g} mode intensity variation with twist angles reflects the interplay of interlayer interaction and proximity effects. As the A_{1g} mode belongs to Γ point in the Brillouin zone, where the interlayer hybridization occurs, and 532 nm laser excitation is close to the *B* exciton of WS_2 (Table S2), the absorption and peak intensity for WS_2 are highest at ~0.5° twist in the WS_2/WSe_2. This intensity decreases with excitonic detuning (Fig. 2e). The resonance Raman effect becomes prominent when excitation energy falls between van Hove singularities (vHS) that promote band nesting and enhance Raman intensity.[42] The extracted intensity enhancement factors (EF), defined as the ratio of heterostructure-to-monolayer phonon mode intensities, shows that for WSe_2 in WS_2/WSe_2, EF of A_{1g} increases from ~0.5º, peaks at ~40º with ~80 fold enhancement compared to 0.5º, and then decreases (Fig. 2f). EF remains higher at 60° than at 0° due to stacking-dependent band structure modification. In homobilayer WSe_2, the *C* exciton/E_{vHS} of the *2H* (60º) phase is closer to 532nm excitation than in the 3R phase (0°) at room temperature. A similar trend is seen in in-plane modes, such as [$2LA(M)+E_{2g}(\Gamma)$] of WS_2 and *2LA(M)* of WSe_2, due to higher absorbance near resonance excitation (Fig. S7). For MoS_2 and $MoSe_2$, $A(X_0)$, *B*, and *C* excitonic transitions (Table S2) are far from the laser excitation, making resonance Raman effects negligible in $MoS_2/MoSe_2$, MoS_2/WSe_2 and $WS_2/MoSe_2$ (Figs. 2g-i,l). However, WSe_2 and WS_2 show the enhancement characteristics (Figs. 2j,k). Therefore, the critical angle, θ_C, at which the 532nm excitation falls within the vHS of WSe_2 in twisted LHBs lies within 30°<θ<40º, amplifying vibrational intensity via the resonant Raman process.

Charge-Transfer Dynamics, Excitonic & Degree-of-Valley Polarization Modulation:

The particular TMDs hetero-bilayers exhibit type-II band alignment, enabling interlayer charge transfer and exciton formation (Fig. 4a). The excitons can be further trapped within the moiré potential (Fig. 4b). To investigate charge-transfer dynamics, first-principles calculations using Badar charge analysis were performed, endowing electron transfer from WSe_2 or $MoSe_2$ to WS_2 or MoS_2 (Figs. 4c, S8a). Since the A_{1g} mode is sensitive to carrier concentration, its peak position variation with twist angle provides insights into charge transfer. Generally, electron (hole) doping in 1L TMDs results in a redshift (blueshift)

of the A_{1g} mode. For WS_2/WSe_2,consistent with simulated differential charge density plots (Fig. 4c), the A_{1g} mode of WS_2 redshifts at angle-aligned stacking (~0.5° and~ 60°), indicating electron transfers from WS_2 to WSe_2. Interestingly, the expected blue shift in WSe_2 is absent, possibly due to the substantial lattice relaxation (Fig. 4d). Similar charge transfer behavior is observed in other hetero-bilayers, such as the A_{1g} blueshifts in $MoSe_2$ (Fig. S8b).

The twist angle-dependent intralayer exciton intensity variations in LHBs were analyzed to reaffirm the resonance Raman effects at room temperature. Excitonic photoluminescence (PL) spectra show that WSe_2 exhibits lower (higher) PL intensity for $0^o<\theta<20^o$ ($20^o<\theta<60^o$) as compared to WS_2 and MoS_2 (Figs. 4e,S9). In WS_2/WSe_2, the *A*-exciton intensity ratio of WSe_2-to-WS_2 increases from ~0.2 in $0^o<\theta<20^o$ to ~3 in $20^o< \theta<60^o$, while no significant and systematic variation is observed in $MoS_2/MoSe_2$ and $WS_2/MoSe_2$ (Figs. 4f,S9). Thus, Raman intensity variation and enhancement due to the resonant Raman process correlates with PL intensity changes, reflecting twist-angle dependent optical absorption. Specifically, for WSe_2, following phonon mode intensity variation, higher absorption is expected for $30^o<\theta<40^o$. However, a direct quantitative relation cannot be drawn since the intralayer *A*-excitons follow the *k-k* transitions, whereas the *C* excitons are centered at the Γ valley. To further investigate hetero-strain effects on intralayer and interlayer excitonic response in moiré potential, PL measurements were performed down to 5K, focusing on $MoS_2/MoSe_2$ and WS_2/WSe_2. Coupling in the heterostructure manifests as PL intensity quenching and excitonic resonance shifts. In $MoSe_2$, the *A* exciton peak splits into multiple resonances, a signature of moiré intralayer excitons (Figs. 4g,h).

The degree of valley polarization (DOCP) for MoS_2 decreases in hetero-bilayers compared to its 1L, while for $MoSe_2$, it enhances (Figs. 4i-j, S10). The DOCP reduction in MoS_2 is possibly attributed to selective strain-associated chiral phonon generation and *k-k´* inter-valley scattering[15]. In contrast, the enhancement in $MoSe_2$ is linked to moiré potential localization, which reduces intralayer electron-hole Coulomb exchange interactions and increases intralayer valley lifetimes[45,46]. For WS_2/WSe_2, the DOCP modulationaligns with the phononic picture (Figs. 4l, S11c). Interestingly, WS_2 and WSe_2 exhibit enhanced DOCP in hetero-bilayers compared to their 1Ls. While the selective strain effect is pronounced on WSe_2 and should reduce DOCP, the dominant moiré potential counteracts this effect, leading to an overall enhancement. A recent theoretical study in WS_2/WSe_2 predicted valley polarization enhancement for WSe_2 as high as 90% at small twist angles but did not account for lattice relaxation[45]. In our case, the competition between strain and moiré effects results in valley polarization of excitons reaching up to 20% and 40%. For interlayer exciton, a redshift in energy and an enhancement in DOCP occur as the twist angle decreases, consistent with higher moiré confinement (Fig. 4k). The direct interlayer excitonic transitions are theoretically simulated and fall within the telecom wavelength range (Table S3), highlighting the potential of these LHBs for designing quantum emissions for quantum communications in telecom windows.

SHG Modulation:

SHG mapping of hetero-bilayers reveals the influence of moiré materials and strain on nonlinear optical phenomena (Figs. 1e,5d-f). In CVD-grown TMDs, 1L flakes predominantly form triangular or hexagonal islands with crystal edges, aiding orientation while stacking two LHSs. This alignment matches SHG-determined angles (Fig. S11) without requiring additional identification tools. The SHG intensity for all four hetero-bilayers gradually decreases with increasing twist angle due to the dephasing of the coherent superposition of SHG fields from two individual layers (Fig. 5a)[33,47]. Surprisingly, an SHG enhancement is observed in $WS_2/MoSe_2$ at ~60º, despite the expected destructive interference (Fig. 5f). This anomaly may

arise from strain generation due to lattice reconstruction, which breaks the symmetry and detunes out-of-phase coincidence, consistent with phonon spectra trends (Figs. 2d). In contrast, no such enhancement is observed in the other three hetero-bilayers. Further investigation through SHG intensity variation of individual TMDs and hetero-bilayers reveals that the WSe_2 domains exhibit the highest SHG intensity, whereas $MoSe_2$ is the least intense. MoS_2 and $MoSe_2$ show similar intensities (Fig. 5b). Quantitatively, WSe_2 is ~500% brighter, while MoS_2 and WS_2 are 50% brighter than $MoSe_2$. These variations in SHG modulation highlight the role of tuning and detuning of SHG photon energy with excitonic resonance[48].

The second-order susceptibility peaks when SHG photon energy resonates with the excitonic transition. In this study, the 2.95 eV SHG photon energy aligns with the D exciton of WSe_2, promoting resonance enhancement. Across the four hetero-bilayers, systematic engineering of SHG intensity in the matting layer can be observed due to sensitizer (Fig. 5b) and phase mismatch (Fig. 5c). This SHG modulation arises from two primary mechanisms: (1) interlayer coherence, governed by the orbital characteristics of each layer, which modulates the combined non-centrosymmetric effect, and (2) band-offset-driven phase matching/delay, where large offsets increase phase delay and reduced SHG intensity. WS_2/WSe_2 exhibits strong SHG enhancement due to similar orbital characteristics of transition metals and a lower band offset between the D exciton of WSe_2 and the C exciton of WS_2 (Table S2), reducing the phase delay. In $MoS_2/MoSe_2$, despite matching orbital characteristics, higher band offsets cause higher dephasing, limiting SHG enhancement[49]. In MoS_2/WSe_2, large orbital mismatching suppresses its lower band-offset benefits, preventing significant SHG enhancement. $WS_2/MoSe_2$ experiences maximum phase delay and unfavorable orbital overlap, minimizing overall SHG. However, at 60º, lattice reconstruction in $WS_2/MoSe_2$ introduces sufficient strain to detune interlayer coherence from out of phase, turning on SHG (Figs. 5f,g).

To understand phase mismatch variations between the LHBs in moiré networks and anomalous enhancement of SHG at 60º for $WS_2/MoSe_2$, we have simulated the electronic band structure of the four hetero-bilayer systems. While the three systems exhibit direct bandgaps, $WS_2/MoSe_2$ in AB stacking shows an indirect bandgap (Fig. 5g,h), resulting in a greater phase delay for two SHG photons to coherently combine into one photon. These findings highlight that, beyond twist angle, orbital

characteristics between two stacked layer, band offset, strain, and their degree of simultaneity are crucial factors in tuning interlayer coherence.

Conclusion

This study demonstrates the impact of twist angle and material engineering on the optical properties of multi-moiré networks in LHBs-based vdW heterostructures. The findings reveal that, beyond interlayer rotational alignment, the orbital characteristics of interfacing atoms play a crucial role in phonon dynamics, strain distribution, and atomic reconstruction. WS_2/WSe_2 and $MoS_2/MoSe_2$ heterostructures exhibit the highest local strain for twist angles of $0°<\theta<3º$, while MoS_2/WSe_2 and $WS_2/MoSe_2$ experience maximum strain at$0°<\theta<1º$. This suggests that in TMDs hetero-bilayers, homo-transition metal interfaces promote stronger interlayer coupling, while hetero-transition metal combinations more effectively induce a pronounced moiré effect. In addition, local torsional strain is more pronounced in the softer crystal at small twist angles, while local volumetric strain dominates in the top layer at larger angles in moiré networks. Specific interlayer twists can manifest resonance effects, amplifying the intensity of Raman modes. The study further establishes that orbital characteristics and excitonic resonance offsets modulate interlayer coherence and nonlinear optical properties. Persistent strain can break the symmetry, leading to enhanced nonlinear optical responses. These insights deepen the understanding of complex vdW heterostructures and highlight Raman spectroscopy as a powerful tool for probing structural, optical, and hybridization effects in 2D multi-moiré platforms.

This work provides a strategic framework for engineering novel 2D quantum materials and advancing the quantitative understanding of twisted vdWs heterojunctions in one platform. The findings open pathways for developing phonon engineering-driven quantum thermal devices, nanoscale excitonic lattices, arrays of moiré optoelectronic systems, and broadband SHG-based photonic applications.

Methods

Synthesis:

All in-plane MoS_2-WS_2 and $MoSe_2$-WSe_2 lateral hetero-monolayers were synthesized employing a one-pot sequential edge epitaxial CVD approach. This method utilized selective thermal evaporation of solid precursors under atmospheric pressure at different carrier gas environments[34]. Bulk powders of $MoSe_2$ and WSe_2 were used as solid sources to grow Se-based LHS, while MoS_2 and WS_2 were used for the MoS_2-WS_2 heterostructures. Both combinations of precursors were placed together within a high-purity alumina boat in a 2:1 ratio and kept inside a 1-inch quartz tube placed horizontally on a two-zone furnace. At 6-10 cm downstream from the boat (maintained at 1050ºC), cleaned SiO_2/Si (285 nm oxide thickness) substrates were placed for the TMDs deposition in a temperature window of 750-800ºC. Initially, the furnace temperature was raised slowly to 1050ºC in 100 minutes under a constant flow of nitrogen (N_2) at a rate of 200 standard cubic centimeters per minute (sccm). Once the furnace reached

1020ºC, the boat and substrate were inserted at their designated position by sliding the furnace. Simultaneously, water vapor was introduced to oxidize the precursor by diverting N_2 through a water bubbler. After a preferred time to switch growth from Mo to W-based chalcogenides, the N_2+ H_2O gas was replaced with Ar+H_2(5%). After finishing growth, the furnace was further pushed to keep the substrate at a lower temperature under a continuous flow of Ar+H_2(5%) up to cooling down to room temperature.

2D Transfer:

For the vertical heterostructuring, water-mediated pickup and dry transfer of CVD-grown LHSs using PDMS were carried out (Fig S2). CVD-grown samples are more adhesive to the substrate and difficult to tear from the same. To minimize substrate adhesion, we injected water vapor with the flakes at the interface between the PDMS and the substrate. After a preferred time, the PDMS was slowly delinked; during this period, water molecules interacted to loosen the stickiness to the substrate and help to pick up the flakes onto the PDMS. After picking up the desired flake onto PDMS and aligning it with another flake at certain twist angles, the transfer was made to fabricate hetero-bilayers. H-BN flakes were mechanically exfoliated on PDMS to cap the hetero-bilayers and transferred onto the existing hetero stack. The samples were annealed under a 10^{-3} mbar vacuum at 200ºC for 2hr to ensure strong coupling. For 5K PL measurements, h-BN encapsulation was done via successive pickup and transfer.

Computational Details:

The structural and electronic properties of the hetero-bilayers were explored by Density Functional Theory (DFT) using plane wave basis, as implemented in the Vienna Ab initio Simulation Package (VASP) code[50]. The electron interactions were accounted by Perdew-Burke-Ernzerhof (PBE) exchange-correlations functionals with the generalized gradient approximation (GGA)[51]. The vdWs correction was included by the DFT+D3 method as implemented in VASP[52,53]. A vacuum space of 25 A^o was given in the z-direction to avoid the interlayer interaction between the periodically stacked layers. The kinetic energy cut-off was set to 520 eV. A 11X11X1 Monkhorst-Pack (MP) k-mesh was used to sample the Brillouin zone (BZ). The structure was fully optimized until the total energy and forces on each atom between two consecutive steps became less than 10^{-6} eV and 0.001 eV, respectively.

The phononic properties of the hetero-bilayers were calculated using the finite displacement method implemented in the Phonopy package with VASP as the force calculator[54,55]. During all the phonon calculations, we used a supercell of 2X2X1 of LBHs with 24 atoms. The kinetic energy cut-off for the plane-wave basis sets was set to 800 eV, and for sampling the BZ, a 7X7X1 MP k-mesh was used.

Optical measurements:

All room temperature Raman and Photoluminescence measurements were conducted in a confocal micro-Raman system (Renishaw) in the backscattering geometry under the 532 nm laser line as the

excitation source. A 100X objective with 0.95 numerical aperture (NA) was used for focusing and collecting the scattered light. For the Raman signal dispersion, a 2400 grooves per mm diffraction grating and a charge-coupled-device (CCD) having liquid-nitrogen-cooling was used for its detection. The spectral resolution was 0.3 cm^{-1}. The laser power was kept at 40 μW in all the measurements to avoid the laser-induced heating of the materials.

Cryogenic Photoluminescence spectroscopy was performed in a home-built confocal system with a 532 nm laser line and objective of NA = 0.82 in a cryogen-free closed-cycle cryostat (Attodry800) at T = 4.89 K. To acquire the spectra a 0.5 m focal length spectrometer and water-cooled CCD was used on a 150 lines/mm grating with a spectral resolution of ~2.5 meV. The laser power was kept at 100 μW for all the measurements. For the polarization-resolved PL measurements, circularly polarized light was used to selectively excite a particular valley of the material, and the circularly polarized PL emissions were collected by using a quarter–wave plate, a half-waveplate, and a linear polarizer in front of the spectrometer.

Polarization-resolved SHG measurements were performed to determine the twist angle between two 1L lateral heterostructures. In our measurements, we performed the SHG intensity mapping, varying the polarization of the laser together with detection polarization from 0° to 360° (with steps of 5°). The LHBs were excited with an 840 nm linearly polarized femtosecond laser (Mira Optima 900-F-Coherent) at a 76 MHz repetition rate. SHG intensity as a function of excitation laser polarization was recorded at 420 nm by a PMT. By comparing the SHG response from the individual monolayers, the twist angle of the LHBs is determined. The laser beam with 8 mW power was focused on the sample by a 40X objective with NA = 0.95. We used 560 nm and 690 nm short-pass filters to block the laser reflection. The measured angles from SHG are well matched with the measured angles from two parallel lines via an optical microscope with accuracy.

For the SHG mapping, the samples were scanned by the laser using a set of galvanometric mirrors (LaVison BioTec) in a Nikon microscope with a spatial resolution of approximately 1 μm. The SHG intensities were analyzed using the Image-J software.

To calculate the phase mismatch, we use the following equations;

$$I = I_1 + I_2 + 2\sqrt{I_1 I_2}\cos\delta$$

$$\delta = \cos^{-1}\left[\frac{I - (I_1 + I_2)}{2\sqrt{I_1 I_2}}\right]$$

where d is the relative phase difference between the SHG field of the two interfacing 1Ls. I_1 and I_2 are the SHG intensity corresponding to the individual monolayers, and I is the SHG intensity from the stacked region of these two TMDs.

TEM measurements:

Standard PMMA-assisted wet transfer was carried out to transfer the stacked sample onto the TEM grid. The measurement was performed at 300 kV in a JEOL JEM-ARM300F2 microscope with an aberration-correction, cold-field emission gun, and JEOL HAADF detector. For the HAADF-STEM imaging, 20 µs per pixel scan speed was used at the probe size of 8c.

Photoemission Spectroscopy:

Angle-resolved photoemission spectroscopy with micro-scale spatial resolution (mARPES) was performed at the SGM4 beamline of the ASTRID2 synchrotron radiation source at Aarhus University, Denmark[56]. Prepared vertical heterostructure samples were annealed at room temperature under a chamber pressure of 5×10^{-8} mbar prior to the ARPES measurements. The samples were measured at a base pressure of $<1\times10^{-10}$ mbar at room temperature. SPECS Phoibos 150 SAL analyzer was used for the ARPES spectra collection. Keeping the sample at a fixed position and using the scanning angle lens feature of the analyzer, the energy, and momentum resolved (E, k_x, k_y) photoemission intensity measurements were done under the photon energy of 56 eV at linear horizontal was applied for the ARPES measurements. A capillary mirror was used to focus the beam down to a spot size of 4 µm. The energy and angular resolutions were higher than 35 meV and 0.01 $Å^{-1}$, respectively, throughout the measurement. Angle to momentum coordinates transformation, and a Fermi level correction was carried out on the raw ARPES spectra based on reference spectra of gold measured at the same experimental conditions. Wave Metrics IGOR Pro 7 software was used for data plotting and analyses.

Declarations

Acknowledgement:

PS acknowledges the Department of Science and Technology (DST), India (Project Code: DST/NM/TUE/QM-1/2019; DST/TDT/AMT/2021/003 (G)&(C)), and ISIRD start-up grant (ISIRD/2019-2020/23) from the Indian Institute of Technology Kharagpur. TEM work was performed at Sophisticated Analytical Technical Help Institute (SATHI), IIT Kharagpur, supported by DST, Govt of India. SK acknowledges DST, India (Project code: DST/NM/TUE/QM-2/2019) and the matching grant from IIT Goa. IDP acknowledges The Council of Scientific & Industrial Research (CSIR), New Delhi, for the doctoral fellowship. SB and SD thank IISER Tirupati for Intramural Funding and SERB, Dept. of Science and Technology (DST), Govt. of India for research grant CRG/2021/001731. GKP acknowledges the use of the micro-Raman facility at the Central Research Facility (CRF) of KIIT Deemed to be University, Bhubaneswar, and also thanks the Science and Engineering Board (SERB) for financial support (CRG/2020/006190). SB and SD acknowledge National Supercomputing Mission (NSM) for providing computing resources of ‘PARAM Brahma’; at IISER Pune, which is implemented by C-DAC and supported by the Ministry of Electronics and Information Technology (MeitY) and DST, Govt. of India. CS and SU

acknowledge funding from the European Research Council (ERC) under the grant “EXCITE” (grant no. 101124619).

Author contributions:

SC carried out the synthesis, transfer, stacking, STEM sample preparation and room-temperature optical measurements. IDP and SK conducted the low-temperature photoluminescence measurements. FBS and RR performed SHG measurements under the supervision of LMM. SB and SD provided theoretical simulations. PR, BN, and BK helped with CVD process development. CS, SU, AJ, and JM performed μARPES measurements. SC carried out all analyses with input from PS. SC and PS wrote the manuscript with inputs from CS, SK, SD, LMM, and GP. PS initiated and supervised the project. All authors participated in discussing the results and reviewing the manuscript.

References

1. Nuckolls, K. P. & Yazdani, A. A microscopic perspective on moiré materials. *Nat. Rev. Mater.* **9**, 460–480 (2024).
2. Du, L. *et al.* Nonlinear physics of moiré superlattices. *Nat. Mater.* **23**, 1179–1192 (2024).
3. Oudich, M., Kong, X., Zhang, T., Qiu, C. & Jing, Y. Engineered moiré photonic and phononic superlattices. *Nat. Mater.* **23**, 1169–1178 (2024).
4. Barré, E. *et al.* Engineering interlayer hybridization in van der Waals bilayers. *Nat. Rev. Mater.* **9**, 499–508 (2024).
5. Du, L. *et al.* Moiré photonics and optoelectronics. *Science* **379**, eadg0014 (2023).
6. Huang, D., Choi, J., Shih, C.-K. & Li, X. Excitons in semiconductor moiré superlattices. *Nat. Nanotechnol.* **17**, 227–238 (2022).
7. Stansbury, C. H. *et al.* Visualizing electron localization of WS_2/WSe_2 moiré superlattices in momentum space. *Sci. Adv.* **7**, eabf4387 (2021).
8. Gu, J. *et al.* Remote imprinting of moiré lattices. *Nat. Mater.* **23**, 219–223 (2024).
9. Blundo, E. *et al.* Localisation-to-delocalisation transition of moiré excitons in $WSe_2/MoSe_2$ heterostructures. *Nat. Commun.* **15**, 1057 (2024).
10. Susarla, S. *et al.* Hyperspectral imaging of exciton confinement within a moiré unit cell with a subnanometer electron probe. *Science* **378**, 1235–1239 (2022).
11. McRae, A. C. *et al.* Mechanical Control of Quantum Transport in Graphene. *Adv. Mater.* **36**, 2313629 (2024).
12. Park, H. *et al.* Dipole ladders with large Hubbard interaction in a moiré exciton lattice. *Nat. Phys.* **19**, 1286–1292 (2023).
13. Xiong, R. *et al.* Correlated insulator of excitons in WSe_2/WS_2 moiré superlattices. *Science* **380**, 860–864 (2023).

14. Bai, Y. *et al.* Excitons in strain-induced one-dimensional moiré potentials at transition metal dichalcogenide heterojunctions. *Nat. Mater.* **19**, 1068–1073 (2020).
15. Pan, Y. & Caruso, F. Strain-induced activation of chiral-phonon emission in monolayer WS2. *Npj 2D Mater. Appl.* **8**, 1–7 (2024).
16. Lian, Z. *et al.* Valley-polarized excitonic Mott insulator in WS_2/WSe_2 moiré superlattice. *Nat. Phys.* **20**, 34–39 (2024).
17. Wang, X. *et al.* Light-induced ferromagnetism in moiré superlattices. *Nature* **604**, 468–473 (2022).
18. Lin, Q. *et al.* Moiré-engineered light-matter interactions in MoS2/WSe_2 heterobilayers at room temperature. *Nat. Commun.* **15**, 8762 (2024).
19. Lian, Z. *et al.* Quadrupolar excitons and hybridized interlayer Mott insulator in a trilayer moiré superlattice. *Nat. Commun.* **14**, 4604 (2023).
20. Tagarelli, F. *et al.* Electrical control of hybrid exciton transport in a van der Waals heterostructure. *Nat. Photonics* **17**, 615–621 (2023).
21. Kim, J. *et al.* Anomalous optical excitations from arrays of whirlpooled lattice distortions in moiré superlattices. *Nat. Mater.* **21**, 890–895 (2022).
22. Birkbeck, J. *et al.* Quantum twisting microscopy of phonons in twisted bilayer graphene. *Nature* 1–7 (2025).
23. Chen, D. *et al.* Tuning moiré excitons and correlated electronic states through layer degree of freedom. *Nat. Commun.* **13**, 4810 (2022).
24. Naik, M. H. *et al.* Intralayer charge-transfer moiré excitons in van der Waals superlattices. *Nature* **609**, 52–57 (2022).
25. Chatterjee, S. *et al.* Harmonic to anharmonic tuning of moiré potential leading to unconventional Stark effect and giant dipolar repulsion in WS_2/WSe_2 heterobilayer. *Nat. Commun.* **14**, 4679 (2023).
26. Quan, J. *et al.* Phonon renormalization in reconstructed MoS_2 moiré superlattices. *Nat. Mater.* **20**, 1100–1105 (2021).
27. Li, Y. *et al.* Coherent Modulation of Two-Dimensional Moiré States with On-Chip THz Waves. *Nano Lett.* **24**, 12156–12162 (2024).
28. Ramos-Alonso, A., Remez, B., Bennett, D., Fernandes, R. M. & Ochoa, H. Flat and Tunable Moir\'e Phonons in Twisted Transition-Metal Dichalcogenides. *Phys. Rev. Lett.* **134**, 026501 (2025).
29. Qin, Z. *et al.* Moiré Pattern Controlled Phonon Polarizer Based on Twisted Graphene. *Adv. Mater.* **36**, 2312176 (2024).
30. Yoon, Y. *et al.* Terahertz phonon engineering with van der Waals heterostructures. *Nature* **631**, 771–776 (2024).
31. Qin, T., Zhou, J. & Shi, J. Berry curvature and the phonon Hall effect. *Phys. Rev. B* **86**, 104305 (2012).
32. Maity, I., Mostofi, A. A. & Lischner, J. Chiral valley phonons and flat phonon bands in moir\'e materials. *Phys. Rev. B* **105**, L041408 (2022).

33. Lin, K.-Q. *et al.* Twist-angle engineering of excitonic quantum interference and optical nonlinearities in stacked 2D semiconductors. *Nat. Commun.* **12**, 1553 (2021).
34. Sahoo, P. K., Memaran, S., Xin, Y., Balicas, L. & Gutiérrez, H. R. One-pot growth of two-dimensional lateral heterostructures via sequential edge-epitaxy. *Nature* **553**, 63–67 (2018).
35. Sousa, F. B., Lafeta, L., Cadore, A. R., Sahoo, P. K. & Malard, L. M. Revealing atomically sharp interfaces of two-dimensional lateral heterostructures by second harmonic generation. *2D Mater.* **8**, 035051 (2021).
36. Wilson, N. R. *et al.* Determination of band offsets, hybridization, and exciton binding in 2D semiconductor heterostructures. *Sci. Adv.* **3**, e1601832 (2017).
37. Xiang, Q. *et al.* Unveiling the origin of anomalous low-frequency Raman mode in CVD-grown monolayer WS2. *Nano Res.* **14**, 4314–4320 (2021).
38. Van Winkle, M. *et al.* Rotational and dilational reconstruction in transition metal dichalcogenide moiré bilayers. *Nat. Commun.* **14**, 2989 (2023).
39. Bhatnagar, M. *et al.* Temperature induced modulation of resonant Raman scattering in bilayer 2H-MoS_2. *Sci. Rep.* **12**, 14169 (2022).
40. Kim, K., Lee, J.-U., Nam, D. & Cheong, H. Davydov Splitting and Excitonic Resonance Effects in Raman Spectra of Few-Layer $MoSe_2$. *ACS Nano* **10**, 8113–8120 (2016).
41. del Corro, E. *et al.* Atypical Exciton–Phonon Interactions in WS2 and WSe2 Monolayers Revealed by Resonance Raman Spectroscopy. *Nano Lett.* **16**, 2363–2368 (2016).
42. Rahman, S., Sun, X., Zhu, Y. & Lu, Y. Extraordinary Phonon Displacement and Giant Resonance Raman Enhancement in WSe_2/WS_2 Moiré Heterostructures. *ACS Nano* **16**, 21505–21517 (2022).
43. Mignuzzi, S. *et al.* Effect of disorder on Raman scattering of single-layer MoS_2. *Phys. Rev. B* **91**, 195411 (2015).
44. An, H. *et al.* Tip-Enhanced Raman Spectroscopy of Monolayer MoS_2 on Au(111). *J. Phys. Chem. C* **128**, 7583–7590 (2024).
45. Wang, R., Chang, K., Duan, W., Xu, Y. & Tang, P. Twist-Angle-Dependent Valley Polarization of Intralayer Moir\'e Excitons in van der Waals Superlattices. *Phys. Rev. Lett.* **134**, 026904 (2025).
46. Dai, D. *et al.* Twist angle–dependent valley polarization switching in heterostructures. *Sci. Adv.* **10**, eado1281 (2024).
47. Hsu, W.-T. *et al.* Second Harmonic Generation from Artificially Stacked Transition Metal Dichalcogenide Twisted Bilayers. *ACS Nano* **8**, 2951–2958 (2014).
48. Kim, W. *et al.* Exciton-Sensitized Second-Harmonic Generation in 2D Heterostructures. *ACS Nano* **17**, 20580–20588 (2023).
49. Le, C. T. *et al.* Effects of Interlayer Coupling and Band Offset on Second Harmonic Generation in Vertical $MoS_2/MoS_{2(1-x)}Se_{2x}$ Structures. *ACS Nano* **14**, 4366–4373 (2020).
50. Kresse, G. & Furthmüller, J. Efficient iterative schemes for ab initio total-energy calculations using a plane-wave basis set. *Phys. Rev. B* **54**, 11169–11186 (1996).

51. Perdew, J. P., Burke, K. & Ernzerhof, M. Generalized Gradient Approximation Made Simple. *Phys. Rev. Lett.* **77**, 3865–3868 (1996).
52. Grimme, S., Antony, J., Ehrlich, S. & Krieg, H. A consistent and accurate ab initio parametrization of density functional dispersion correction (DFT-D) for the 94 elements H-Pu. *J. Chem. Phys.* **132**, 154104 (2010).
53. Grimme, S., Ehrlich, S. & Goerigk, L. Effect of the damping function in dispersion corrected density functional theory. *J. Comput. Chem.* **32**, 1456–1465 (2011).
54. Togo, A., Oba, F. & Tanaka, I. First-principles calculations of the ferroelastic transition between rutile-type and $CaCl_2$-type SiO_2 at high pressures. *Phys. Rev. B* **78**, 134106 (2008).
55. Togo, A. & Tanaka, I. First principles phonon calculations in materials science. *Scr. Mater.* **108**, 1–5 (2015).
56. Jones, A. J. H. *et al.* A spatial- and angle-resolved photoemission spectroscopy beamline based on capillary optics at ASTRID2. *Rev. Sci. Instrum.* **96**, 025109 (2025).

Figures

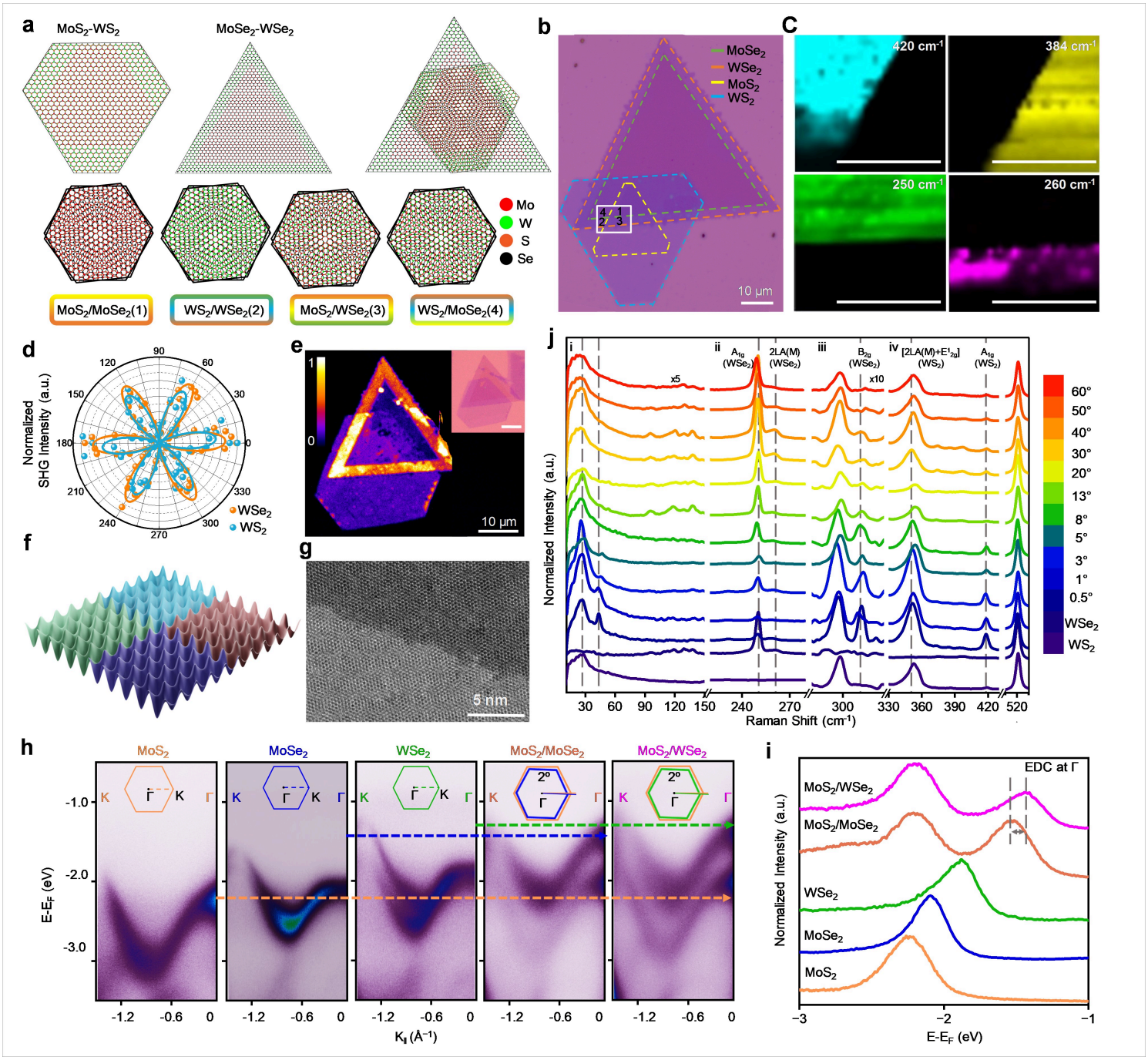


Figure 1

Multi-Moiré Networks on Engineered 2D Lateral Hetero-Monolayers: *(a) Schematic representation of multi-moiré networks on monolayer 2D lateral heterostructure platforms. Stacking of LHSs forms WS_2/WSe_2, $WS_2/MoSe_2$, $MoS_2/MoSe_2$, and MoS_2/WSe_2; the four pockets of heterogeneous lateral hetero-bilayers (LHBs) in a single sample geometry. (b) Optical microscopic image of a twisted heterogeneous bilayer of LHBs, composed of MoS_2-WS_2 and $MoSe_2$-WSe_2, where the color contrast indicates the different domains. $MoSe_2$ (green), WSe_2 (orange), MoS_2 (yellow), and WS_2 (blue) regions are denoted by the dashed lines. The four different moiré networks are labeled with 1-4, following the assigned numbers in* ***a****. (c) Spatially resolved Raman spectral intensity mapping for the marked region*

*with a white rectangular box in **b** showing the spatial distribution of four moiré networks and the uniform coupling throughout the areas (scale bar 10 μm). (d) Polarization-dependent SHG signal of a 2.7º twisted LHB sample. (e) SHG intensity mapping at 420nm of the sample in **d**. The intensity differences between the moiré networks show the difference in interfacial coupling effect on non-centrosymmetry. (f) Schematic representation of the four pockets of moiré potentials. (g) Atomic-resolution z-contrast HAADF-STEM image showing the formation of different moiré networks across the 1D interface with different color contrast. (h) Energy- and momentum-resolved band dispersion obtained from μARPES measurements along the high-symmetry Γ-K direction of MoS_2, $MoSe_2$, WSe_2, $MoS_2/MoSe_2$ and MoS_2/WSe_2 (i) Energy distribution curve (EDC) extracted at the Γ-point, showing the effect of interlayer hybridization on the band structure. (j) Full-length Raman spectra at different twist angles for WS_2/WSe_2 compared to monolayer WS_2 and WSe_2.*

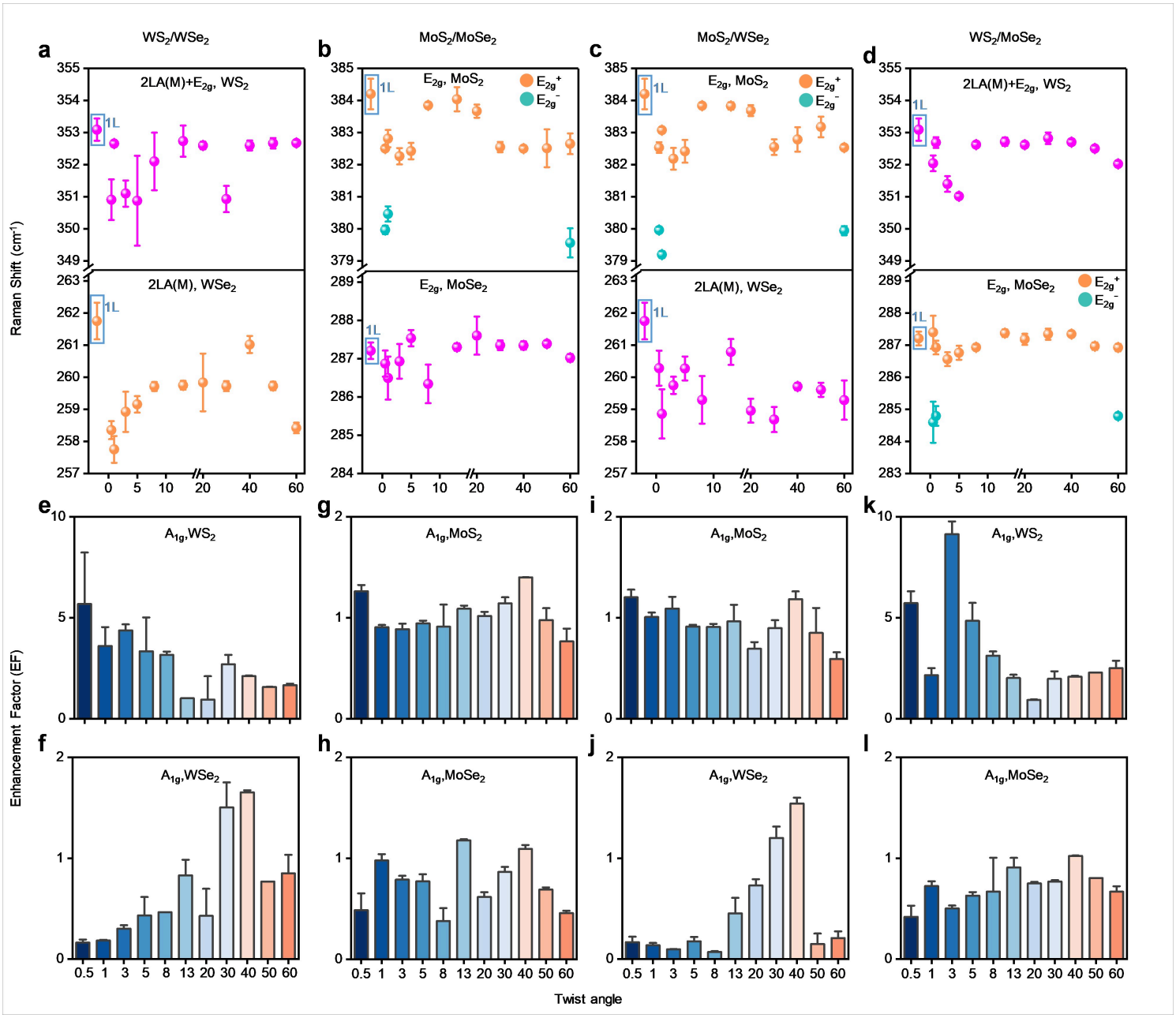


Figure 2

Material and twist angle engineered phonon frequency and intensity renormalization: *Peak position/ frequency variation of in-plane phonon -modes as a function of twist angle to individual TMDs for the (a) WS_2/WSe_2: [2LA(M)+ E^1_{2g}] of WS_2 and 2LA(M) of WSe_2, (b) $MoS_2/MoSe_2$: E^1_{2g} of MoS_2 and $MoSe_2$. (c) MoS_2/WSe_2: E^1_{2g} of MoS_2 and 2LA(M) of WSe_2. (d) $WS_2/MoSe_2$: [2LA(M)+ E^1_{2g}] of WS_2 and E^1_{2g} of $MoSe_2$. Large displacement and splitting of the phonon peaks for the specific TMDs in each moiré network [2LA(M) of WSe_2 in WS_2/WSe_2, E^1_{2g} of MoS_2 in both $MoS_2/MoSe_2$ and MoS_2/WSe_2, E^1_{2g} of $MoSe_2$ in $WS_2/MoSe_2$] with stacking angle is largely influenced by the rotational reconstruction driven local strain in the Moiré superlattice and selective on the mechanically softer crystal. All Raman spectra are normalized to the Si frequency of 521 cm^{-1}. The error bar corresponds to the data from multiple samples and multiple point measurements at a certain twist to eliminate stacking order fluctuations and the sample's inhomogeneity. (e-l) Enhancement factor (EF) of the A_{1g} mode for the four individual TMDs in moiré networks. EF is extracted from the intensity ratio in the heterostructure to that in the monolayer with normalization to Si peak (521 cm^{-1}) intensity.*

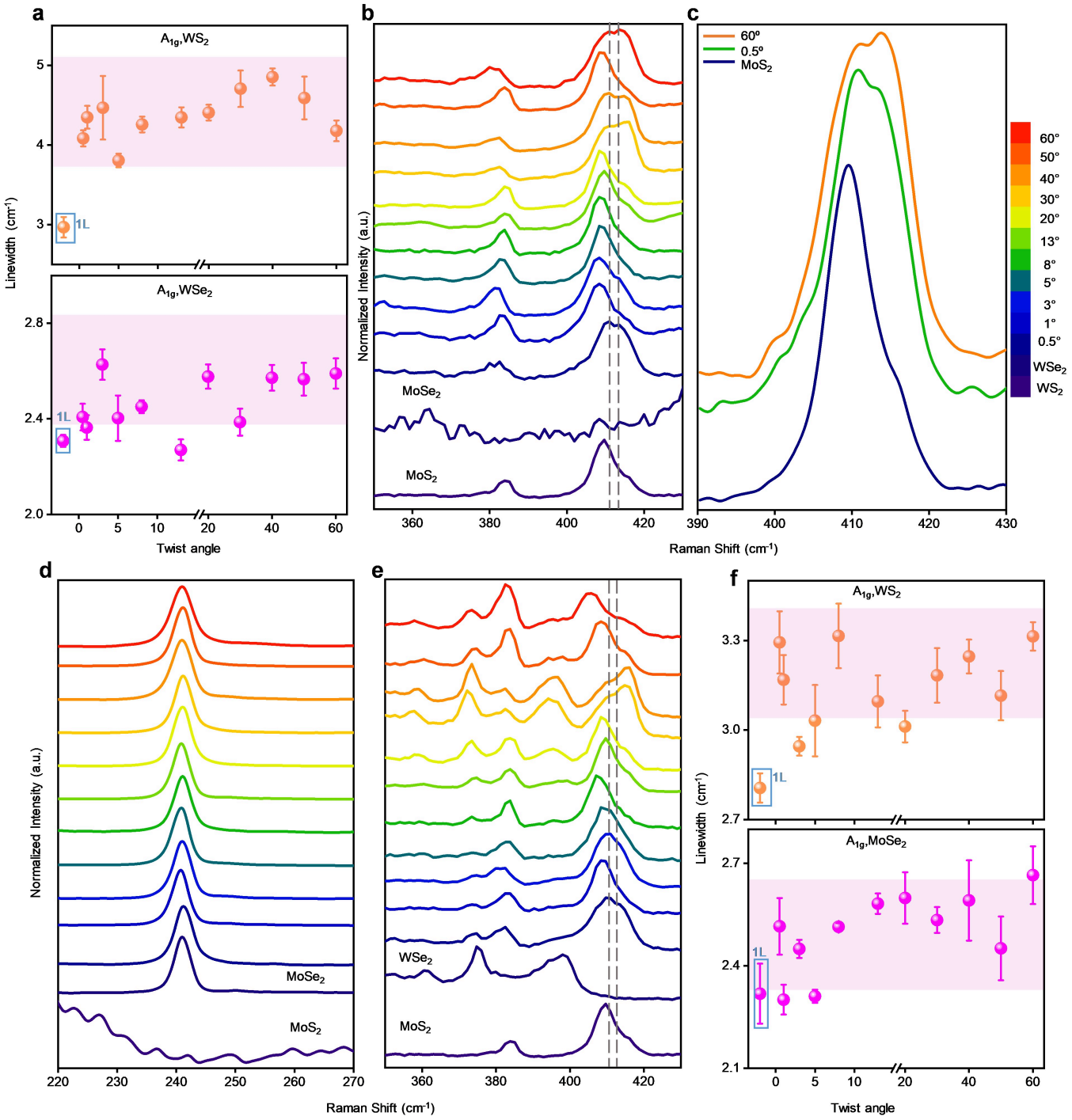


Figure 3

Twist angle and moiré material controlled out-of-plane phonon-mode (A_{1g}) linewidth engineering: *(a) Twist angle dependent linewidth variation in A_{1g} mode of WS_2 and WSe_2 in WS_2/WSe_2 system. For WS_2, the linewidth broadens by 1 cm^{-1} window, whereas WSe_2 holds it at <0.4 cm^{-1}. The broadening in out-of-plane mode indicates the local volumetric strain is robust on the top layer WS_2 following epitaxial*

pseudo-morphism. (b) Raman spectra of $MoS_2/MoSe_2$ combination in the range of 330-430 cm^{-1} showing fuzziness in A_{1g} mode line-shape of MoS_2. Since strain from lattice relaxation is pronounced on MoS_2 for both modes, it activates some forbidden modes in the spectrum to make it fuzzy. (c) Signature of Davydov splitting (splitting of A_{1g} into two modes with a separation of 3 cm^{-1}) at ~0.5º and ~60º with opposite intensity ratio. The symmetry breaking and distinctness from local torsional strain originate the splitting. The shoulder peak in 1L could originate from the non-Γ-point phonon modes in the ZO branch[43,44]. (d) Raman spectra of $MoS_2/MoSe_2$ within 220-280 cm^{-1} showing no broadening in A_{1g} mode line-shape for $MoSe_2$. (e) Raman spectra of MoS_2/WSe_2 combination within 330-430 cm^{-1} showing similar line shape characteristics for MoS_2 A_{1g} mode as in $MoS_2/MoSe_2$. However, the splitting of A_{1g} is only present at 0.5º with less distinctness due to reduced interlayer coupling from hetero-transition metal. (f) A_{1g} mode linewidth evolution for the individuals in $WS_2/MoSe_2$ combination.

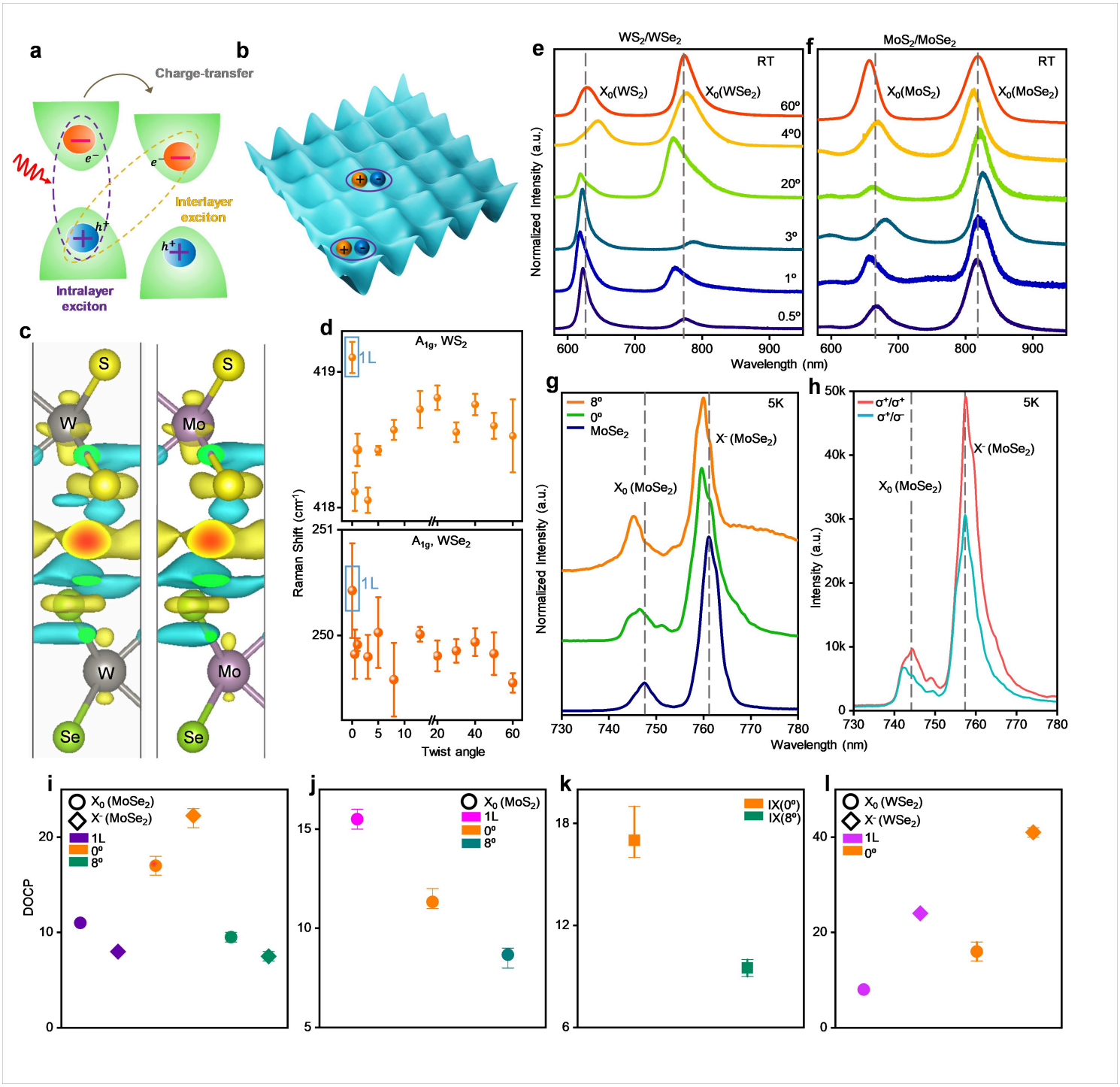


Figure 4

Photoluminescence & Valley Polarization characteristics: *(a) Schematic representation of charge transfer in a vdW heterostructure via type-II band alignment showing the formation of intralayer and interlayer exciton under photo-excitation. (b) The periodic modulation of the electrostatic potential in the twisted hetero-bilayers due to the moiré superlattice results in the trapping of excitons in the moiré potential. (c) The differential charge density plot of WS_2/WSe_2 and $MoS_2/MoSe_2$ hetero-bilayers. The cyan and yellow colors denote electron depletion and accumulation regions, respectively. Badar charge analysis shows charge transfer from WSe_2 to WS_2 and $MoSe_2$ to MoS_2. (d) A_{1g} mode peak position*

variation with twist angle for WS_2 and WSe_2 within heterobilayer as a signature of charge transfer. The redshift of A_{1g} mode in WS_2 compared to monolayer correlates with electron doping. With increasing twist angle, the amount of redshift decreases due to decreased charge transfer efficiency from momentum mismatch. For WSe_2, the insignificant redshift is a signature of the local strain effect that dominates over the charge transfer-driven electron-withdrawing effect. (e-f) Room temperature PL response for WS_2/WSe_2 and $MoS_2/MoSe_2$. (g) PL response at 5K and (h) The circularly polarized PL spectra of intralayer exciton and trion at 0º with respect to monolayer for $MoS_2/MoSe_2$. (i-l) degree of valley polarization (DOCP) variation of exciton and trion at different twist angles within hetero-bilayers, compared to their monolayer counterpart.

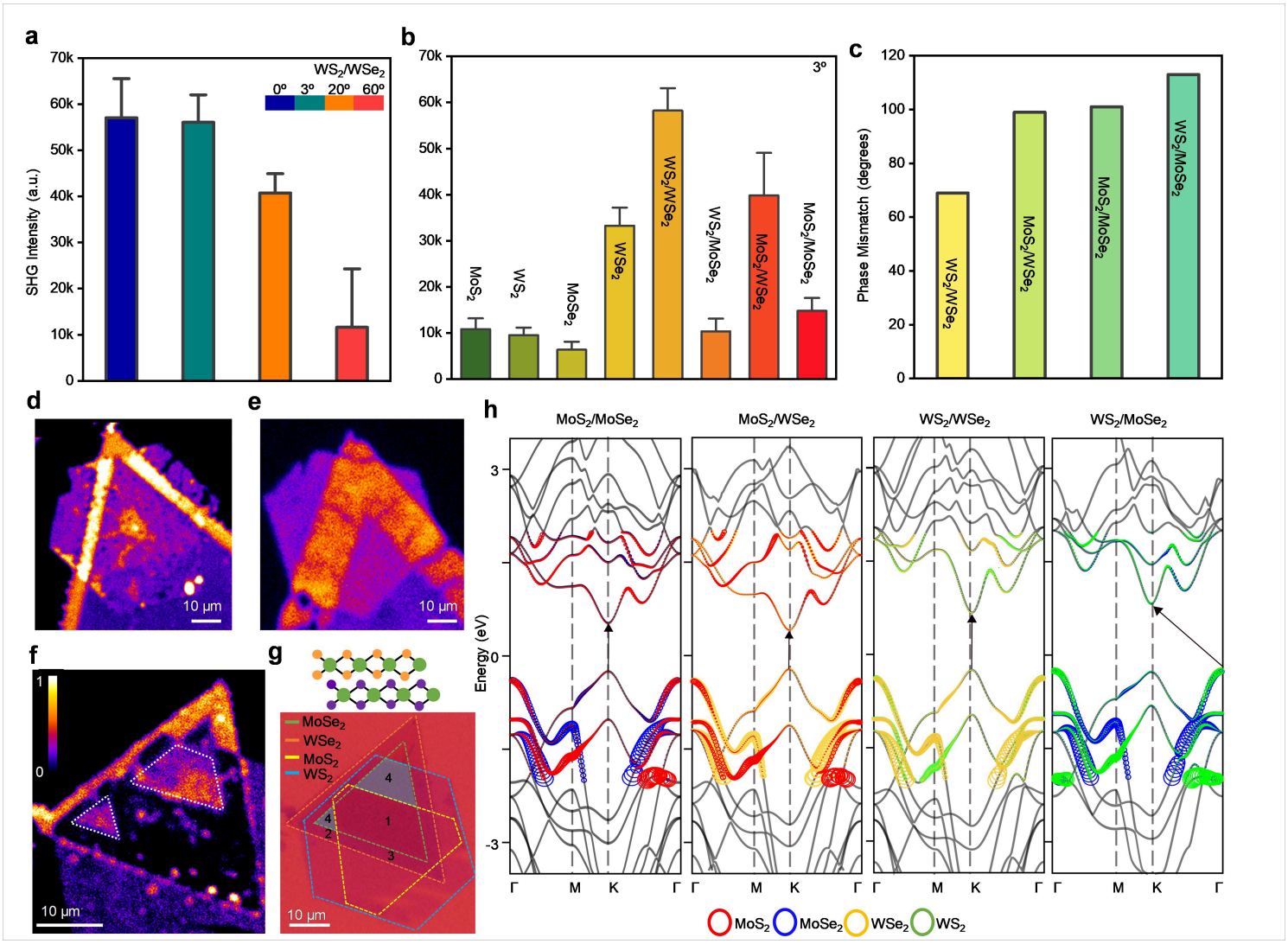


Figure 5

Second harmonic response modulation across different moiré networks: *(a) Twist angle dependent SHG intensity variation for WS_2/WSe_2 system. With increasing twist angle, the SHG intensity decreases due to the reduced interlayer coherency. Similar characteristics hold for other moiré networks. (b) Individual TMD and moiré networks specific SHG intensity variation at ~3º. The variation in the intensity for the individual TMDs is related to the excitation-tuned second-order susceptibility and symmetry breaking.*

For the individual moiré networks, the variation is related to excitonic-resonance offset and coherency in orbital characteristics controlled combined non-centrosymmetric effect where WS_2/WSe_2 has the highest and $WS_2/MoSe_2$ is the least intense domains. (c) Calculated phase-mismatch for the individual moiré networks from the intensity variation. $WS_2/MoSe_2$ has the highest phase delay. (d-f) SHG intensity mapping at different angles. At a constant angle, the mapping shows the distribution of intensities corresponding to the four moiré networks. For the mapping in ***f****, though the other three stacked regions show complete suppression of the SHG intensity, the intensity is not diminished in the region marked with white dashed lines. (g) Schematic of 2H or AB-like stacking order. Optical image of the stacked sample with an angle of 58.7º (2H-like stacking) and SHG mapping in* ***f****. The highlighted region with indexing 4 corresponding to white marked in* ***f*** *is $WS_2/MoSe_2$. (h) Simulated band structure for the four moiré networks in AB configurations. The calculated band profile shows that, unlike WS_2/WSe_2, $MoS_2/MoSe_2$, and MoS_2/WSe_2 maintaining a direct band gap nature, $WS_2/MoSe_2$ transformed to an indirect band gap.*

Supplementary Files

This is a list of supplementary files associated with this preprint. Click to download.

- SIMoirePhononXSumanetal.IITKgp.pdf